Efficiency improvement of the femtosecond laser source of superponderomotive electrons and X-ray radiation due to the use of near-critical density targets

N.E. Andreev, V.S. Popov, O.N. Rosmej, A.A. Kuzmin, A.A. Shaykin, E.A. Khazanov, A.V. Kotov, N.G. Borisenko, M.V. Starodubtsev, A.A. Soloviev

Abstract. **We consider the possibility of improving the superhigh-power laser pulse to superponderomotive electrons energy conversion efficiency by using porous targets of near-critical density. We report the results of numerical simulations based on the typical parameters of laser pulses of the PEARL laser facility built on the principles of parametric chirped pulse amplification (OPCPA). An original scheme for producing a controllable prepulse based on the use of a pump laser switched to a two-pulse regime is discussed. The prepulse is required to homogenise the submicron inhomogeneities of a porous target. Simulations show a significant increase in the laser-to-electron energy conversion efficiency in comparison with solid-state and gas targets. This interaction regime can be used to improve the efficiency of a broad class of laser-driven secondary radiation sources, such as a betatron source, bremsstrahlung, neutron source, etc.**

Keywords: laser-plasma interaction, near-critical density plasma, laser-plasma PEARL facility, controlled prepulse, efficient sources of secondary radiation.

1. Introduction

Relativistic electron beams generated in the course of laser-plasma interactions are a powerful tool for producing bright ultrashort sources of gamma-ray radiation [1–4] as well as X-ray synchrotron radiation [5–8]. The efficiency of laser-plasma sources of radiation and particles is primarily determined by the efficiency of energy transfer from a laser pulse to electrons. There are different mechanisms for the transfer of laser energy to high-energy 'hot' electrons (superponderomotive electrons), depending on the parameters of the laser and the type of the target.

Target densities can be in a wide range – from solid to tenuous gas densities. In addition, a variety of target topologies are employed: targets with a sharp and distributed boundary, cluster targets, layered targets, capillaries, etc. The heating mechanisms of solid-state density targets strongly depend on the gradients of the preplasma at the target surface. These can be vacuum heating [9], resonant absorption in critical density plasma, ponderomotive and ($J \times B$) acceleration mechanisms [10, 11], stochastic heating [12–15], etc. The interaction of laser radiation with low-density gas targets provides efficient acceleration of electrons to high energies in the wake fields generated in plasma channels [16–18]. In this case, significant results have been achieved in the area of monoenergetic electron beam generation. For example, the energies obtained in experiments on the interaction of relativistic laser pulses with low-density gas jets and capillary plasma are in the range from hundreds of MeV to several GeV [19–23]. However, it is possible to accelerate a relatively small number of electrons. The electron beam charges in LWFA experiments do not exceed several hundred pC [23–25].

One of the possibilities to increase the electron beam charge above the nanocoulomb level with retention of electron energy at a level from tens to hundreds of MeV consists in using relativistic laser interaction with a near-critical density (NCD) plasma [26–28]. The critical electron density is defined as $n_{cr} = m\omega_{las}^2/(4\pi e^2)$, where m and e are the mass of an electron at rest and its charge, and ω_{las}^2 is the laser radiation frequency. One of the first theoretical works discussing the particle acceleration in relativistic laser channels generated in a plasma with a near-critical density is based on the results of 3D PIC simulations [29]. The simulations demonstrated the channelling and filamentation of a relativistic laser pulse in expanding channels with a near-critical density and the generation of a high current of electrons with an energy of 10–100 MeV, a Maxwellian energy distribution, and an effective temperature, which, among other things, depends on the intensity of laser radiation and the length of the plasma region with near-critical density.

The mechanism of electron acceleration in an NCD plasma has a complex nature, since it simultaneously includes several physical processes. Pukhov et al. [29] proposed a mechanism for the direct interaction of the laser field with hot electrons in relativistic laser channels. The implementation of

N.E. Andreev Joint Institute for High Temperatures, Russian Academy of Sciences, Izhorskaya ul. 13, stroenie 2, 125412 Moscow, Russia; Institute of Applied Physics, Russian Academy of Sciences, ul. Ul'yanova, 46, 603950 Nizhny Novgorod, Russia;
V.S. Popov Joint Institute for High Temperatures, Russian Academy of Sciences, Izhorskaya ul. 13, stroenie 2, 125412 Moscow, Russia;
O.N. Rosmej GSI Helmholtz Centre for Heavy Ion Research, Planckstraße 1, 64220 Darmstadt, Germany; Goethe-University, Institute of Applied Physics, Max-von-Laue-Straße 1, 60438 Frankfurt am Main, Germany;
A.A. Kuzmin, A.A. Shaykin, E.A. Khazanov, A.V. Kotov, M.V. Starodubtsev, A.A. Soloviev Institute of Applied Physics, Russian Academy of Sciences, ul. Ulyanova 46, 603950 Nizhny Novgorod, Russia; e-mail: 7oloviev@gmail.com;
N.G. Borisenko Lebedev Physical Institute, Russian Academy of Sciences, Leninsky prosp. 53, 119991 Moscow, Russia

this mechanism requires strong self-generated static electric and magnetic fields that hold fast electrons in relativistic channels. In these fields, electrons experience transverse betatron oscillations, which ensure efficient energy exchange when the betatron frequency becomes close to the laser radiation frequency shifted due to the Doppler effect [29].

Following Pukhov et al.' work, an extended analysis of the interaction of a relativistic laser pulse with a subcritical plasma was carried out by Arefiev et al. [30] and Khudik et al. [31]. They investigated the direct laser acceleration (DLA) of relativistic electrons experiencing betatron oscillations in the plasma channel, as well as the role of transverse and longitudinal quasi-static electric fields. In Ref. [31], a universal scaling was obtained analytically for the maximum attainable electron energy.

Despite all the obvious efficiency of interaction with NCD targets, their experimental implementation is associated with a number of technical difficulties that hinder research. For radiation pulses of the optical range, the near-critical density in a gas jet is achieved at a technically difficult input pressure of hundreds and thousands of atmospheres. At the same time, homogeneous liquid or solid substances with a near-critical density do not exist due to the smallness of the characteristic scale of the action of covalent chemical bonds. One way to obtain near-critical densities is to use solid-state microstructured targets, whose average density is reduced due to the presence of cavities in them. Such targets require the development of specific production technologies, and, in addition, the very interaction with a high-power laser driver should occur some time after ionisation, so that the hydrodynamic expansion of the fine structure of the target could smooth out the density nonuniformity of the preformed plasma. This brings up the problem of providing preliminary ionisation for the preparation of a uniform plasma.

So far, only a few experiments have been performed using a high-power PW laser with a subpicosecond pulse duration [28, 32, 33] to demonstrate the advantages of the DLA mechanism in plasma with a near-critical electron density. In the experiments under description, ultrarelativistic electron beams were produced in the interaction of subpicosecond laser pulses with an intensity of the order of 10^{19} W cm^{-2} with an NCD plasma prepared using a nanosecond pedestal [28] or a separate nanosecond pulse that generated a supersonic ionisation wave in low-density foam polymers [32, 33]. These experiments showed a strong increase in the efficiency of conversion of the laser pulse energy into the energy of superponderomotive electrons. In addition, in Ref. [33], where bremsstrahlung in the energy range corresponding to tens of megaelectronvolts was generated by the interaction of DLA electrons with a golden converter, a record value (1.2%) of the conversion efficiency of laser pulse energy into gamma-ray radiation energy exceeding 1 MeV. The possibility of generating ultrabright betatron radiation in a plasma channel, where relativistic electrons perform transverse betatron oscillations in quasi-static fields, was shown in PIC modelling for the case of a subpicosecond laser pulse and a radiation intensity of 10^{19} W cm^{-2} [34].

At the same time, of great interest are the feasibility studies of advancing to the region of shorter (femtosecond) laser pulse durations. This area is interesting in that higher pulse repetition rates are available in it due to the lower energy and, as a consequence, the applied significance of research increases. Promising results in the production of betatron and gamma-ray radiation in the exposure of near-critical density targets to laser pulses tens of femtoseconds in duration and at least 10^{21} W cm^{-2} in intensity were obtained theoretically in Refs [35–37]. However, so far experimental interaction studies have not been carried out for these parameters, and adequate scaling to femtosecond pulses has not been obtained, which calls for numerical simulations with parameters close to experimental ones.

The aim of this work is full-scale numerical simulation of the interaction of a femtosecond laser pulse with NCD targets for parameters typical for the PEARL laser facility [38]. Since it is well known that nanostructures in plasma can significantly affect the interaction regime [39], special emphasis is placed on the practical aspect of preparing a homogeneous plasma from a porous target. Plasma of near-critical density is prepared several nanoseconds before the arrival of a high-power laser pulse using nanosecond radiation from the pump laser of the PEARL facility, which is switched to the original double-pulse regime.

The expected efficient increase in the laser to superponderomotive electron energy conversion efficiency when using extended porous targets can form the basis for new efficient laser-driven sources of fast particles and X-ray radiation.

2. Production of near-critical density targets

Obtaining a uniform hydrodynamically stable layer of NCD plasma remains an urgent task. 3D PIC simulations of the interaction of relativistically intense laser radiation with large-scale NCD plasmas [26, 27] suggest that low-density polymer airgel [40–42] is a highly promising material for producing submillimetre-thick NCD plasma and efficient electron acceleration in it.

To obtain a homogeneous plasma with a high aspect ratio (the thickness of the formed plasma layer is much greater than the width) and an electron density slightly below the critical one, use can be made of polymer airgel layers with a density of 2 mg cm^{-3} and thicknesses of 300 and 500 μm [40–42]. Airgel foams are optically transparent and are characterised by a very uniform three-dimensional reticular microstructure with a thickness of 0.1 μm, consisting of pores 1–2 μm in size and 1 μm fibres with a density of about 0.1 g cm^{-3}. Density fluctuations over an area of 100×100 μm do not exceed 0.5%. Due to the open cell structure, the air contained in the pores can be removed. An average foam volume density of 2 mg cm^{-3} corresponds to 1.7×10^{20} atoms per cm^{-3} and an average ion charge $Z_{mean} = 4.2$. When a nanosecond laser pulse that produces a plasma interacts with the surface of the foam, the solid membranes/fibres ionise. The plasma generated by ionisation of fibres with a density of 0.1 g cm^{-3} (8×10^{21} atoms per cm^{-3}) and a thickness of 100 nm has a supercritical electron density, while the fibre thickness is greater than the skin layer thickness (~ 30 nm). Therefore, it takes time for the resultant plasma to expand into the pores. As a result, the subcritical electron density is reached and further propagation of the laser pulse into the three-dimensional structure of the airgel occurs. The intensity of a nanosecond pulse producing a plasma can be matched to the density and thickness of the target [32, 43] so that the velocity of the ionisation front is much higher than the velocity of ionic sound. In this case, during the propagation of the supersonic ionisation wave, the heated plasma region with a large aspect ratio does not undergo a noticeable expansion.

3. Parameters of the laser facility

The basis of the PEARL laser-plasma facility is a femtosecond laser OPCPA system [38] with the centre wavelength of 910 nm. At the compressor output, the laser pulse has an aperture of ~180 mm, a duration of less than 60 fs, and an energy of 15–25 J in the regime without significant degradation of optical elements. If necessary, by realigning the stretcher–compressor system, the pulse duration can be readily increased with retention of its energy by introducing linear frequency modulation into the pulse. The use of an adaptive wavefront correction system makes it possible to achieve focusing with a Strehl number $S = 0.6$ [44, 45] and higher. When using a parabolic mirror with a focal length of 75 cm, taking into account the residual phase aberrations, the characteristic radius of the radiation intensity distribution at the focus will be 3.5 μm at the e^{-2} level, which will make it possible to obtain radiation intensity up to 10^{21} W cm^{-2} (20 J, 60 fs). The contrast ratio of the laser system is, according to Ref. [46], 2×10^8 on a time scale of 0.5 ns and is satisfactory for experiments with near-critical density targets.

4. Preionisation of the target

For controlled preionisation of the target, we plan to use a nanosecond pump laser converted to the original double-pulse operation regime [47, 48]. This regime is based on the separation of a pump radiation pulse at a wavelength of 1054 nm in front of power amplifiers into two replicas with different polarisations and a controlled energy ratio. As a result of an effective increase in the pulse duration, such a configuration allows one, on the one hand, to reduce the distortion of the temporal envelope during amplification in the saturation regime, and, on the other hand, to extract additional energy from the amplifier stages, remaining below the radiation damage threshold of the optical elements [47, 49].

The double-pulse regime was developed for pumping additional parametric amplifier stages due to a more complete use of the energy stored in glass active elements while maintaining their number and architecture of the laser facility. Due to the polarisation separation of the pulses, the double-pulse regime can be readily adapted for laser-plasma interaction in the regime of a controlled nanosecond prepulse. In this case, one of the pulses will be used for the preionisation of the porous target, and the other for pumping the parametric amplifier.

A schematic of controllable prepulse production is shown in Fig. 1.

The use of the PEARL facility for generating the prepulse of a nanosecond pump laser permits solving several problems simultaneously: to ensure timing of the prepulse with the high-power femtosecond pulse with the possibility of controlling the delay between them and to provide prepulse energy from several to hundreds of joules.

The PEARL facility is based on parametric amplification and has therefore been designed with the highest demands on the temporal stability of the signal pulse relative to the pump pulse. The initial electrical timing system provides 50 ps jitter between the signal pulse and the pump pulse [50]. The upgrade of the system planned for the near future using optical timing approaches [51] will further reduce jitter to a subpicosecond
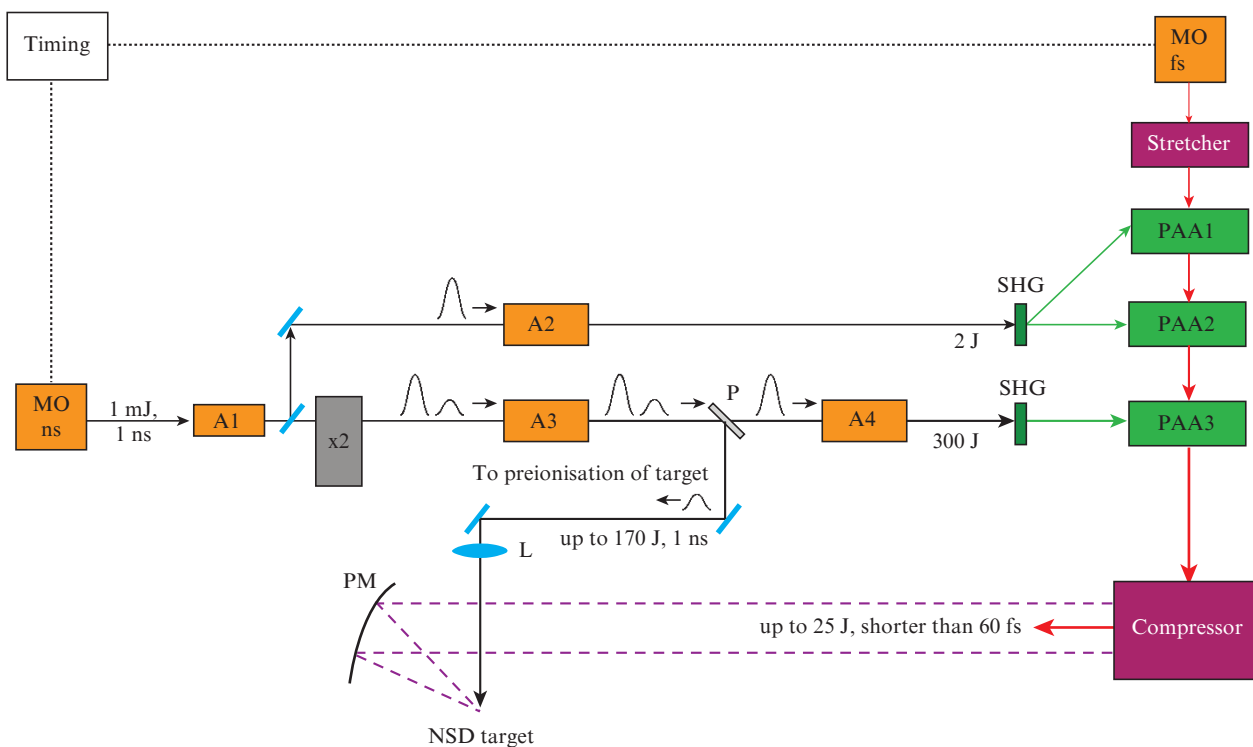

Figure 1. Block diagram of the production of a controlled nanosecond prepulse in the PEARL laser facility:
(MO fs and MO ns) femtosecond and nanosecond master oscillators; (PAA) parametric amplifiers; (A) neodymium pump amplifiers (Nd: YAG: A1 and A2; neodymium-doped phosphate glass: A3 and A4); (SHG) second harmonic generator; (P) polariser; (x2) double-pulse shaping system; (L) lens for focusing nanosecond prepulse; (PM) off-axis parabolic mirror for focusing femtosecond pulses. Focusing and compression take place in vacuum chambers (not shown in the figure).

level. Therefore, no additional measures are required to synchronise the pulses at the target. A fine change in the delay between femtosecond and nanosecond pulses can be introduced mechanically by changing the length of the delay line, which is convenient to place at the beginning of the laser configuration (x2 in Fig. 1), where the pulse energy is several millijoules and the aperture size does not exceed 1 cm.

Note that the use of the double-pulse regime required upgrading the optical isolation of the pump laser configuration. The pulses have different polarisations, and so a standard Faraday isolator is capable of providing optical isolation for only one of the pulses. The PEARL facility uses a Faraday isolator design for an arbitrary polarisation of the radiation pulse [47]. The optical quality of the pump beam after amplification is characterised by the Strehl number $S \approx 0.15$ [48].

5. Numerical simulations

The interaction of laser radiation with a near-critical-density plasma was simulated using a fully relativistic three-dimensional VLPL PIC code [52] for the laser parameters and interaction geometry corresponding to the experiments planned at the PEARL facility. The pulse energy of the focused laser radiation was 15 J. The pulse was assumed to be Gaussian, and the intensity distribution along the beam radius was also assumed to be Gaussian. In this case, 7.5 J is localised in a spot with a diameter of $D_{FWHM} = 4.12$ μm. The pulse duration τ_{FWHM} was 60 fs, which corresponds to the peak intensity $I_0 = 1.2 \times 10^{21}$ W cm^{-2} and the dimensionless amplitude of the laser pulse field $a_0 = eE_y/(m_e c \omega_0) = 30$, where E_y is the amplitude of the electric field of the laser pulse, and ω_0 is its frequency.

A homogeneous plasma consisted of fully ionised carbon, hydrogen, and oxygen ions and electrons with a density $n_e = (1.0 \text{ or } 2.0)n_{cr}$. The simulation took into account the type of ion and ionic fraction in accordance with the chemical composition of cellulose triacetate $C_{12}H_{16}O_8$. The simulation area had dimensions of $128 \times 35 \times 35$ μm. The first 10 and the last 18 μm from the total space of 128 μm in the x direction (the direction of propagation of the laser pulse) were initially free of plasma. The dimensions of the computational cell were 0.05 μm along the x axis and 0.15 μm along the y and z axes. The number of particles per cell in the simulation was 4 for electrons and 1 for ions of each type. The boundary conditions were absorbing for particles and fields in every direction.

Figure 2 shows the results of simulating the energy spectra of accelerated electrons emitted from the computational domain during the entire interaction time ($ct = 200$ μm, where c is the speed of light; t is the time measured from the moment when the maximum of the laser pulse is at the left boundary of the target). Up to an energy of about 70 MeV, the number of accelerated electrons and their energy distribution practically coincide (to within 10%) for both target electron densities, $n_e = 1.0n_{cr}$ and $2.0n_{cr}$. However, for energies exceeding 100 MeV, the number of accelerated electrons in the lower-density target ($n_e = 1.0n_{cr}$) is several times higher than in the doubled-density target ($n_e = 2.0n_{cr}$) (see Table 1). In this case, for the lower-density target, the electron spectrum in the energy range above 20 MeV can be approximated by a two-temperature distribution with $T_1 \approx 9$ MeV and $T_2 \approx 27$ MeV, and for $n_e = 2.0n_{cr}$ by a distribution with the temperatures $T_1 \approx 6$ MeV and $T_2 \approx 17$ MeV (in the energy range exceeding 10 MeV).
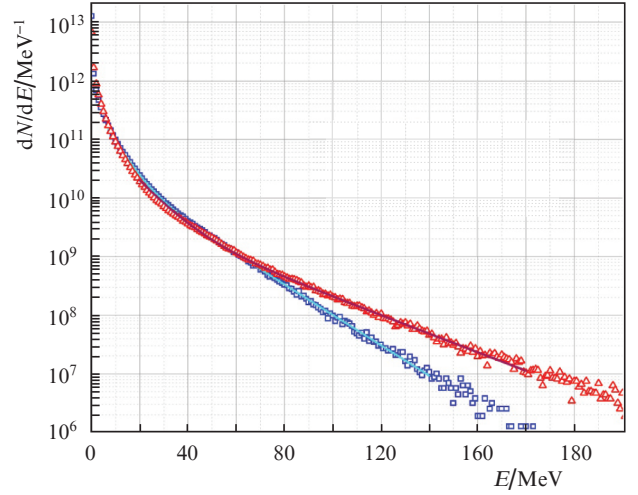
Figure 2. Energy spectra of accelerated electrons for the PEARL parameters (60 fs, $a_0 = 30$) at electron densities of $1.0n_{cr}$ (red triangles) and $2.0n_{cr}$ (blue squares). Solid lines are two-temperature approximations of the spectra with temperatures $T_1 \approx 9$ MeV and $T_2 \approx 27$ MeV for $n_e = 1.0n_{cr}$ and with temperatures $T_1 \approx 6$ MeV and $T_2 \approx 17$ MeV for $n_e = 2.0n_{cr}$.

Figure 3 shows the spectra of accelerated electrons (normalised to the energy of laser pulses) emitted from the computational domain and localised in spots with a diameter D_{FWHM} for the PEARL facility (7.5 J) [38, 39] and for the PHELIX facility (17.5 J, $\tau_{FWHM} = 700$ fs, $D_{FWHM} \approx 10$ μm, $I_0 = 2.5 \times 10^{19}$ W cm^{-2} and $a_0 = 4.3$) [33]. Comparing the spectra presented (see also Table 1) clearly indicates an increase in the efficiency of conversion of the laser pulse energy into the energy of relativistic electrons with increasing intensity, even despite a tenfold decrease in the duration of the PEARL laser pulse relative to the PHELIX pulse.

The angular distributions of electrons emitted from the computational domain with energies exceeding 7 MeV for the target electron density $n_e = 2.0n_{cr}$ are shown in Fig. 4 and for

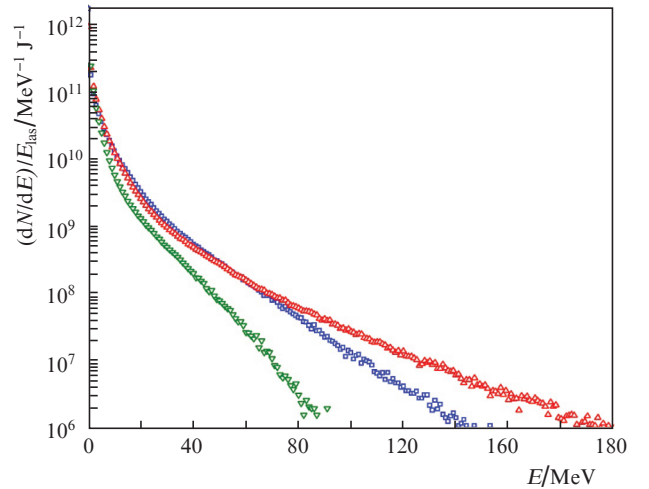**Figure 3.** Energy spectra of accelerated electrons normalised to the laser pulse energy E_{las} for the PEARL parameters ($\tau_{FWHM} = 60$ fs, $a_0 = 30$, $E_{las} = 7.5$ J) for plasma densities $1.0n_{cr}$ (red triangles) and $2.0n_{cr}$ (blue squares) and PHELIX parameters ($\tau_{FWHM} = 700$ fs, $a_0 = 4.3$, $E_{las} = 17.5$ J) for a plasma density of $0.65n_{cr}$ (green triangles).

Table 1. Efficiency of energy transfer of a laser pulse to electrons.

Parameters	PEARL (7.5 J) $n_e = 2.0 n_{cr}$	PEARL (7.5 J) $n_e = 1.0 n_{cr}$	PHELIX (17.5 J) $n_e = 0.65 n_{cr}$	Energy range
Number of electrons per 1 J of laser pulse	3.4×10^{11}	3.5×10^{11}	1.96×10^{11}	$E > 3$ MeV
	1.7×10^{11}	1.5×10^{11}	0.72×10^{11}	$E > 7$ MeV
	1.7×10^{10}	1.7×10^{10}	0.62×10^{10}	$E > 30$ MeV
	2.3×10^{8}	7.5×10^{8}	–	$E > 100$ MeV
Total charge/nC	408	420	510	$E > 3$ MeV
	203	180	187	$E > 7$ MeV
	22	20	15	$E > 30$ MeV
	0.3	0.9	–	$E > 100$ MeV
Energy fraction transferred to electrons	57%	56%	27%	$E > 3$ MeV
	44%	41%	17%	$E > 7$ MeV
	13%	13.5%	3.6%	$E > 30$ MeV
	0.43%	1.6%	–	$E > 100$ MeV

$n_e = 1.0 n_{cr}$ in Fig. 5. When the density is double the critical one, the two brightest spots in the angular distribution in the vertical plane (laser radiation is polarised along the y axis) indicate the decisive role of direct laser acceleration (DLA) [29] in the generation of ultrarelativistic electrons.

With a decrease in the target density ($n_e = 1.0 n_{cr}$) and, accordingly, an increase in the laser pulse–plasma interaction length (in which the pulse is almost completely absorbed), the accelerated electrons are isotropised in the azimuthal angle due to the mutual influence of the relativistic electron motion in the plasma channel in the perpendicular directions Oy and Oz [30], as well as due to the possible additional contribution of the stochastic electron acceleration in the presence of irregular plasma fields [14, 15] (cf. Figs 4 and 5).

The contribution of stochastic acceleration to the generation of high-energy electrons was also discussed in Ref. [53] in the simulation of the interaction of a shorter laser pulse (30 fs) with a more tenuous plasma ($n_e = 1.0 n_{cr}$), where they demon-
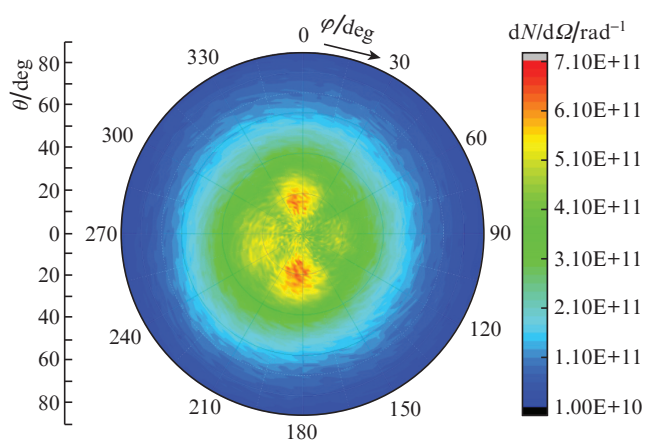
Figure 4. Angular distribution of electrons with energies above 7 MeV (PEARL, $n_e = 2.0 n_{cr}$) emitted into the solid angle element $d\Omega = d\varphi \sin\theta d\theta$ in the direction of propagation of the laser pulse.
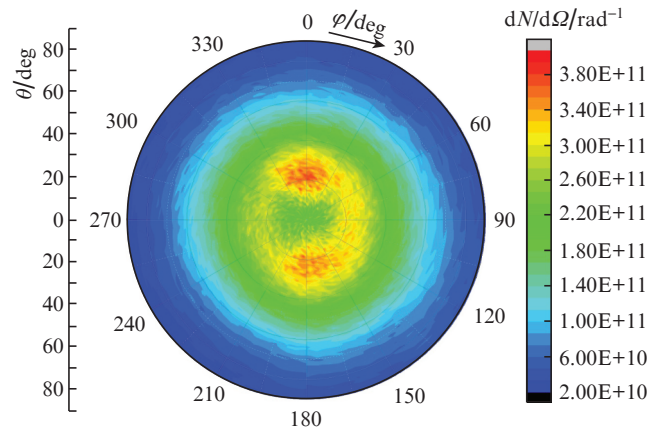
Figure 5. Angular distribution of electrons with energies above 7 MeV (PEARL, $n_e = 1.0 n_{cr}$) emitted into the solid angle element $d\Omega = d\varphi \sin\theta d\theta$ in the direction of propagation of the laser pulse.

strated an efficiency of electron acceleration to energies exceeding 30 MeV, close to our results, with a laser radiation conversion factor of $\sim 15\%$.

6. Conclusions

The results of numerical simulations for the PEARL laser facility demonstrate a high efficiency of direct laser acceleration of electrons from near-critical density targets with electron densities $n_e = 1.0 n_{cr}$ and $2.0 n_{cr}$. In both cases, the energy spectrum of accelerated electrons extends to 150–200 MeV and is described by two effective temperatures, the first of which is close to the ponderomotive potential, and the second exceeds it by two to three times. In this case, the charge of electrons with energies above the ponderomotive energy (11 MeV) is 100 nC for both target densities with electron densities of $1.0 n_{cr}$ and $2.0 n_{cr}$. For a target with $n_e = 1.0 n_{cr}$, the charge of electrons with energies above 100 MeV is 900 pC with a laser pulse energy conversion efficiency of 1.6%, which is three times higher than for a target with $n_e = 2.0 n_{cr}$.

The efficiency of conversion of the laser pulse energy into the energy of relativistic electrons up to 100 MeV is significantly higher than the efficiency both for LWFA and for interactions with solid targets. In particular, electrons with energies above 30 MeV, which are of particular interest for constructing secondary radiation sources on their basis, contain more than 10% of the energy of the laser driver. The simplest version of such a source can be built on the basis of a bremsstrahlung mechanism, for which a converter is located directly behind the NCD target: a layer of atoms with a high charge number Z. The angular spectrum of the bremsstrahlung source will hardly differ from the angular electron distribution and will therefore be highly directional, which is especially important for applications. Secondary X-rays can also be obtained using the undulator mechanism [54] and Thomson backscattering [55]. In addition, a short-pulse neutron source can be implemented on the basis of a superponderomotive electron beam [56, 57].

It is planned to solve the problem of preparing the plasma with the requisite parameters in the laboratory by using airgel targets, which will be ionised by the pulse of the PEARL pump laser switched to an original two-pulse regime.

References

1. Wang T., Ribeyre X., Gong Z., Jansen O., d'Humières E., Stutman D., Toncian T., Arefiev A. *Phys. Rev. Appl.*, **13** (5), 054024 (2020).
2. Norreys P.A., Santala M., Clark E., Zepf M., Watts I., Beg F.N., Krushelnick K., Tatarakis M., Dangor A.E., Fang X., Graham P., McCanny T., Singhal R.P., Ledingham K.W.D., Creswell A., Sanderson D.C.W., Magill J., Machacek A., Wark J.S., Allott R., Kennedy B., Neely D. *Phys. Plasmas*, **6** (5), 2150 (1999).
3. Hatchett S.P., Brown C.G., Cowan T.E., Henry E.A., Johnson J.S., Key M.H., Koch J.A., Langdon A.B., Lasinski B.F., Lee R.W., Mackinnon A.J., Pennington D.M., Perry M.D., Phillips T.W., Roth M., Sangster T.C., Singh M.S., Snavely R.A., Stoyer M.A., Wilks S.C., Yasuike K. *Phys. Plasmas*, **7** (5), 2076 (2000).
4. Zhu X.-L., Chen M., Weng S.-M., Yu T.-P., Wang W.-M., He F., Sheng Z.-M., McKenna P., Jaroszynski D.A., Zhang J. *Science Advances*, **6** (22), eaaz7240 (2020).
5. Kostyukov I., Kiselev S., Pukhov A. *Phys. Plasmas*, **10** (12), 4818 (2003).
6. Kiselev S., Pukhov A., Kostyukov I. *Phys. Rev. Lett.*, **93** (13), 135004 (2004).
7. Rousse A., Phuoc K.T., Shah R., Pukhov A., Lefebvre E., Malka V., Kiselev S., Burgy F., Rousseau J.-P., Umstadter D., Hulin D. *Phys. Rev. Lett.*, **93** (13), 135005 (2004).
8. Cipiccia S., Islam M.R., Ersfeld B., Shanks R.P., Brunetti E., Vieux G., Yang X., Issac R.C., Wiggins S.M., Welsh G.H., Anania M.-P., Maneuski D., Montgomery R., Smith G., Hoek M., Hamilton D.J., Lemos N.R.C., Symes D., Rajeev P.P., Shea V.O., Dias J.M., Jaroszynski D.A. *Nat. Phys.*, **7** (11), 867 (2011).
9. Brunel F. *Phys. Rev. Lett.*, **59** (1), 52 (1987).
10. Wilks S.C., Kruer W.L., Tabak M., Langdon A.B. *Phys. Rev. Lett.*, **69** (9), 1383 (1992).
11. Gibbon P. *Short Pulse Laser Interactions with Matter: An Introduction* (London: Imperial College Press, 2005).
12. Mulser P., Bauer D. *High-Power Laser-Matter Interaction* (Heidelberg: Springer, 2010).
13. Mulser P., Weng S.M., Liseykina T. *Phys. Plasmas*, **19** (4), 043301 (2012).
14. Bochkarev S.G., Brantov A.V., Bychenkov V.Y., Torshin D.V., Kovalev V.F., Baidin G.V., Lykov V.A. *Plasma Phys. Rep.*, **40** (3), 202 (2014).
15. Andreev N.E., Pugachev L.P., Povarnitsyn M.E., Levashov P.R. *Laser Part. Beams*, **34** (1), 115 (2016).
16. Andreev N.E., Kuznetsov S.V., Cros B., Fortov V.E., Maynard G., Mora P. *Plasma Phys. Controlled Fusion*, **53** (1), 014001 (2010).
17. Leemans W.P., Gonsalves A.J., Mao H.-S., Nakamura K., Benedetti C., Schroeder C.B., Tóth Cs., Daniels J., Mittelberger D.E., Bulanov S.S., Vay J.-L., Geddes C.G.R., Esarey E. *Phys. Rev. Lett.*, **113** (24), 245002 (2014).
18. Esarey E., Schroeder C.B., Leemans W.P. *Rev. Modern Phys.*, **81** (3), 1229 (2009).
19. Faure J., Glinec Y., Pukhov A., Kiselev S., Gordienko S., Lefebvre E., Rousseau J.-P., Burgy F., Malka V. *Nature*, **431** (7008), 541 (2004).
20. Pugacheva D.V., Andreev N.E. *Quantum Electron.*, **48** (4), 291 (2018) [*Kvantovaya Elektron.*, **48** (4), 291 (2018)].
21. Walker P.A., Bourgeois N., Rittershofer W., Cowley J., Kajumba N., Maier A.R., Wenz J., Werle C.M., Karsch S., Grüner F., Symes D.R., Rajeev P.P., Hawkes S.J., Chekhlov O., Hooker C.J., Parry B., Tang Y., Hooker S.M. *New J. Phys.*, **15** (4), 045024 (2013).
22. Ju J., Genoud G., Ferrari H.E., Dadoun O., Paradkar B., Svensson K., Wojda F., Burza M., Persson A., Lundh O., Andreev N.E., Wahlström C.-G., Cros B. *Phys. Rev. Spec. Top. Accel Beams*, **17** (5), 051302 (2014).
23. Gonsalves A.J., Nakamura K., Daniels J., Benedetti C., Pieronek C., de Raadt T.C.H., Steinke S., Bin J.H., Bulanov S.S., van Tilborg J., Geddes C.G.R., Schroeder C.B., Tóth C., Esarey E., Swanson K., Fan-Chiang L., Bagdasarov G., Bobrova N., Gasilov V., Korn G., Sasorov P., Leemans W.P. *Phys. Rev. Lett.*, **122** (8), 084801 (2019).
24. Cole J.M., Wood J.C., Lopes N.C., Poder K., Abel R.L., Alatabi S., Bryant J.S.J., Jin A., Kneip S., Mecseki K., Symes D.R., Mangles S.P.D., Najmudin Z. *Sci. Rep.*, **5** (1), 1 (2015).
25. Soloviev A.A., Burdonov K.F., Ginzburg V.N., Gonoskov A.A., Katin E.V., Kim A.V., Kirsanov A.V., Korzhimanov A.V., Kostyukov I.Y., Lozhkarev V.V., Luchinin G.A., Mal'shakov A.N., Martyanov M.A., Nerush E.N., Palashov O.V., Poteomkin A.K., Sergeev A.M., Shaykin A.A., Starodubtsev M.V., Yakovlev I.V., Zelenogorsky V.V., Khazanov E.A. *Nucl. Instrum. Methods Phys. Res., Sect. A*, **653** (1), 35 (2011).
26. Pugachev L.P., Andreev N.E., Levashov P.R., Rosmej O.N. *Nucl. Instrum. Methods Phys. Res., Sect. A*, **829**, 88 (2016).
27. Pugachev L.P., Andreev N.E. *J. Phys. Conf. Ser.*, **1147**, 012080 (2019).
28. Willingale L., Arefiev A.V., Williams G.J., Chen H., Dollar F., Hazi A.U., Maksimchuk A., Manuel M.J.-E., Marley E., Nazarov W., Zhao T.Z., Zulick C. *New J. Phys.*, **20** (9), 093024 (2018).
29. Pukhov A., Sheng Z.M., Meyer-ter-Vehn J. *Phys. Plasmas*, **6** (7), 2847 (1999).
30. Arefiev A.V., Khudik V.N., Robinson A.P.L., Shvets G., Willingale L., Schollmeier M. *Phys. Plasmas*, **23** (5), 056704 (2016).
31. Khudik V., Arefiev A., Zhang X., Shvets G. *Phys. Plasmas*, **23** (10), 103108 (2016).
32. Rosmej O.N., Andreev N.E., Zaehter S., Zahn N., Christ P., Borm B., Radon T., Sokolov A., Pugachev L.P., Khaghani D., Horst F., Borisenko N.G., Sklizkov G., Pimenov V.G. *New J. Phys.*, **21** (4), 043044 (2019).
33. Rosmej O.N., Gyrdymov M., Günther M.M., Andreev N.E., Tavana P., Neumayer P., Zähter S., Zahn N., Popov V.S., Borisenko N.G., Kantsyrev A., Skobliakov A., Panyushkin V., Bogdanov A., Consoli F., Shen X.F., Pukhov A. *Plasma Phys. Controlled Fusion*, **62** (11), 115024 (2020).
34. Shen X.F., Pukhov A., Günther M.M., Rosmej O.N. *Appl. Phys. Lett.*, **118** (13), 134102 (2021).
35. Huang T.W., Robinson A.P.L., Zhou C.T., Qiao B., Liu B., Ruan S.C., He X.T., Norreys P.A. *Phys. Rev. E*, **93** (6), 063203 (2016).
36. Wang H.Y., Liu B., Yan X.Q., Zepf M. *Phys. Plasmas*, **22** (3), 033102 (2015).
37. Brady C.S., Ridgers C.P., Arber T.D., Bell A.R. *Plasma Phys. Controlled Fusion*, **55** (12), 124016 (2013).
38. Lozhkarev V.V., Freidman G.I., Ginzburg V.N., Katin E.V., Khazanov E.A., Kirsanov A.V., Luchinin G.A., Mal'shakov A.N., Martyanov M.A., Palashov O.V., Poteomkin A.K., Sergeev A.M., Shaykin A.A., Yakovlev I.V. *Laser Phys. Lett.*, **4** (6), 421 (2007).
39. Fedeli L., Formenti A., Cialfi L., Pazzaglia A., Passoni M. *Sci. Rep.*, **8** (1), 1 (2018).
40. Khalenkov A.M., Borisenko N.G., Kondrashov V.N., Merkuliev Y., Limpouch J., Pimenov V.G. *Laser Part. Beams*, **24** (2), 283 (2006).

41. Borisenko N.G., Akimova I.V., Gromov A.I., Khalenkov A.M., Merkuliev Yu.A., Kondrashov V.N., Limpouch J., Kuba J., Krousky E., Masek K., Nazarov W., Pimenov V.G. *Fusion Sci. Technol.*, **49** (4), 676 (2006).

42. Borisenko N.G., Khalenkov A.M., Kmetik V., Limpouch J., Merkuliev Y.A., Pimenov V.G. *Fusion Sci. Technol.*, **51** (4), 655 (2007).

43. Gus' kov S.Y., Limpouch J., Nicolaï P., Tikhonchuk V.T. *Phys. Plasmas*, **18** (10), 103114 (2011).

44. Soloviev A.A., Kotov A.V., Perevalov S.E., Esyunin M.V., Starodubtsev M.V., Aleksandrov A.G., Galaktionov I.V., Samarkin V.V., Kudryashov A.V., Ginzburg V.N., Korobeynikova A.P., Kochetkov A.A., Kuzmin A.A., Shaykin A.A., Yakovlev I.V., Khazanov E.A. *Quantum Electron.*, **50** (12), 1115 (2020) [*Kvantovaya Electron.*, **50** (12), 1115 (2020)].

45. Kotov A.V., Perevalov S.E., Starodubtsev M.V., Zemskov R.S., Aleksandrov A.G., Galaktionov I.V., Kudryashov A.V., Samarkin V.V., Soloviev A.A. *Quantum Electron.*, **51** (7), 593 (2021) [*Kvantovaya Electron.*, **51** (7), 593 (2021)].

46. Soloviev A., Burdonov K., Chen S.N., Eremeev A., Korzhimanov A., Pokrovskiy G.V., Pikuz T.A., Revet G., Sladkov A., Ginzburg V., Khazanov E., Kuzmin A., Osmanov R., Shaikin I., Shaykin A., Yakovlev I., Pikuz S., Starodubtsev M., Fuchs J. *Sci. Rep.*, **7** (1), 1 (2017).

47. Shaykin A.A., Kuzmin A.A., Shaikin I.A., Burdonov K.F., Khazanov E.A. *Quantum Electron.*, **46** (4), 371 (2016) [*Kvantovaya Electron.*, **46** (4), 371 (2016)].

48. Kuzmin A.A., Khazanov E.A., Shaykin A.A. *Quantum Electron.* **51** (2), 142 (2021) [*Kvantovaya Electron.*, **51** (2), 142 (2021)].

49. Shaykin A.A. *Quantum Electron.*, **44** (5), 440 (2014) [*Kvantovaya Electron.*, **44** (5), 440 (2014)].

50. Katin E.V., Lozhkarev V.V., Palashov O.V., Khazanov E.A. *Quantum Electron.*, **33** (9), 836 (2003) [*Kvantovaya Electron.*, **33** (9), 836 (2003)].

51. Mukhin I.B., Soloviev A.A., Perevezentsev E.A., Shaykin A.A., Ginzburg V.N., Kuzmin I.V., Mart'yanov M.A., Shaikin I.A., Kuzmin A.A., Mironov S.Yu., Yakovlev I.V., Khazanov E.A. *Quantum Electron.*, **51** (9), 759 (2021) [*Kvantovaya Electron.*, **51** (9), 759 (2021)].

52. Pukhov A. *J. Plasma Phys.*, **61** (3), 425 (1999).

53. Lobok M.G., Brantov A.V., Gozhev D.A., Bychenkov V.Y. *Plasma Phys. Control. Fusion*, **60**, 084010 (2018).

54. Corde S., Ta Phuoc K., Lambert G., Fitour R., Malka V., Rousse A., Beck A., Lefebvre E. *Rev. Mod. Phys.*, **85**, 1 (2013).

55. Schwoerer H., Liesfeld B., Schlenvoigt H.-P., Amthor K.-U., Sauerbrey R. *Phys. Rev. Lett.*, **96**, 014802 (2006).

56. Pomerantz I., McCary E., Meadows A.R., Arefiev A., Bernstein A.C., Chester C., Cortez J., Donovan M.E., Dyer G., Gaul E.W., Hamilton D., Kuk D., Lestrade A.C., Wang C., Ditmire T., Hegelich B.M. *Phys. Rev. Lett.*, **113**, 184801 (2014).

57. Brenner C.M., Mirfayzi S.R., Rusby D.R., Armstrong C., Alejo A., Wilson L.A., Clarke R., Ahmed H., Butler N.M.H., Haddock D., Higginson A., McClymont A., Murphy C., Notley M., Oliver P., Allott R., Hernandez-Gomez C., Kar S., McKenna P., Neely D. *Plasma Phys. Controlled Fusion*, **58**, 014039 (2016). DOI: 10.1088/0741-3335/58/1/014039.